Research Square

Preprints are preliminary reports that have not undergone peer review.
They should not be considered conclusive, used to inform clinical practice,
or referenced by the media as validated information.

Clinorotation-mediated stiffening of Jurkat T-cell-laden lymph node- inspired nanocellulose-alginate 3D-bioprinted droplets

Antonio Minopoli
Università Cattolica del Sacro Cuore
Davide Evangelista
Università Cattolica del Sacro Cuore
Matteo Marras
Università Cattolica del Sacro Cuore
Giordano Perini
giordano.perini@unicatt.it

Università Cattolica del Sacro Cuore
Giada Di Giulio
Università Cattolica del Sacro Cuore
Valentina Palmieri
National Research Council
Giulia Artemi
Agostino Gemelli University Polyclinic
Geny Piro
Agostino Gemelli University Polyclinic
Carmine Carbone
Agostino Gemelli University Polyclinic
Marco De Spirito
Università Cattolica del Sacro Cuore
Massimiliano Papi
Università Cattolica del Sacro Cuore

Research Article

Keywords: 3D bioprinting, nanocellulose-reinforced hydrogels, Jurkat T-cell expansion, clinostat reactor, glioblastoma model

Posted Date: November 6th, 2026

DOI: https://doi.org/10.21203/rs.3.rs-11443928/v1

License: This work is licensed under a Creative Commons Attribution 4.0 International License.
Read Full License

Additional Declarations: No competing interests reported.

Abstract

Three-dimensional bioprinted droplets intended to support immune-cell expansion should reproduce not only the biochemical environment of lymphoid tissues, but also their mechanical and transport-related cues. Here, we developed a simplified lymph node-inspired platform based on droplets bioprinted with a nanocellulose-reinforced alginate bioink which resemble size, shape and stiffness of native lymphoid tissue, and laden with Jurkat cells, used here as a tractable human T-cell line model, and investigated whether clinorotation could promote their flow-mediated mechanical maturation. Droplet motion and surrounding hydrodynamic environment were characterized by video tracking and computational fluid dynamics, whereas local and bulk mechanics were assessed by nanoindentation and rheology after static or dynamic culture. Under the selected rotational regime, the droplets followed stable orbital trajectories within a suspension-based, low-shear environment. Prolonged dynamic conditioning induced marked stiffening of nanocellulose-alginate droplets, as demonstrated by an increase in apparent Young's modulus and higher storage moduli. This response was formulation-dependent and was not reproduced to same extent in alginate hydrogels, indicating that nanocellulose network plays a key role in enabling flow-responsive mechanical maturation. Compared with static controls, dynamically cultured droplets showed higher cell viability, enhanced proliferation, and increased intracellular ATP over 10 days. As proof of concept, dynamically conditioned Jurkat-laden droplets were interfaced with U87 glioblastoma cells in a transwell assay and induced a greater reduction in U87 viability than static droplets or free-cell controls. These findings identify clinorotation as a flow-mediated conditioning strategy capable of promoting mechanical maturation of nanocellulose-reinforced 3D-bioprinted droplets toward the stiffness range of native lymph node while supporting Jurkat T-cell expansion and subsequent immune-tumor interaction studies. The observed biological response likely reflects the integrated contribution of matrix remodeling, hydrodynamic loading, enhanced mass transport, and waste removal.

1. Introduction

Adoptive cell therapies depend on the *ex vivo* generation of large numbers of viable, proliferative, and functionally competent lymphocytes. Despite substantial clinical progress, current manufacturing workflows remain limited by prolonged expansion times, donor-to-donor variability, loss of functional quality during culture, and the difficulty of achieving therapeutically relevant cell yields in a reproducible manner [1–4]. Most expansion protocols are still performed in static or quasi-static systems that only partially reproduce the three-dimensional, mechanically active, and transport-regulated environments in which lymphocyte activation, proliferation, and differentiation normally occur. As cell density increases, the emergence of local oxygen and nutrient gradients, restricted metabolite clearance, and spatially heterogeneous cell-cell interactions can further reduce process efficiency and contribute to variability in the final cellular product.

Three-dimensional bioprinting provides a means of addressing some of these limitations by enabling the controlled fabrication of cell-laden droplets with defined geometry, composition, porosity, and internal

organization [5]. Such platforms are increasingly being developed to recreate tissue-relevant microenvironments for immunology, oncology, and regenerative medicine, including engineered lymphoid niches and in vitro models of immune-tumor interactions [6–10]. This strategy is particularly relevant to T-cell culture because lymphocyte activation and clonal expansion occur physiologically within the lymph node paracortex, where stromal architecture, extracellular matrix organization, interstitial transport, cell confinement, and mechanical cues act in concert to regulate immune-cell behavior. Accordingly, a lymph node-inspired droplet need not reproduce the full cellular and anatomical complexity of a native lymph node to provide a useful experimental platform; rather, it may recapitulate selected structural and biophysical features that are absent from conventional suspension culture [11–15]. To avoid ambiguity, the term “lymph node-inspired” is used throughout in a restricted, biophysical sense. It denotes a three-dimensional lymphocyte-laden droplet construct designed to approximate shape, size, and stiffness range of native lymph node measured here in a murine model. It does not imply reconstruction of lymph-node architecture, stromal and antigen-presenting cell composition, chemokine organization, or immune function.

The choice of biomaterial is central to this approach because the matrix is not merely a passive carrier for encapsulated cells. Its viscoelasticity, poroelasticity, permeability, stress-relaxation behavior, and susceptibility to structural remodeling collectively determine how mechanical forces and soluble factors are transmitted through the droplet. Among printable hydrogel systems, alginate-based bioinks reinforced with cellulose nanofibrils are particularly attractive because they combine cytocompatibility, print fidelity, and structural stability under physiological conditions [16–20]. In these composites, the ionically crosslinked alginate phase provides the hydrated polymer network, whereas nanocellulose introduces a fibrillar reinforcing architecture that enhances mechanical integrity and supports extrusion-based processing. Importantly, cellulose nanofibrils are responsive to hydrodynamic processing: their orientation, packing, and supramolecular organization can be modified by flow, and flow-induced alignment has been associated with increased stiffness and strength in nanocellulose-based materials [21–23]. These properties raise the possibility that nanocellulose-alginate droplets may remain mechanically evolvable after printing and may undergo a form of post-fabrication maturation when exposed to sustained dynamic culture.

This possibility is biologically relevant because T lymphocytes are intrinsically mechanosensitive [24, 25]. Mechanical forces contribute to T-cell receptor engagement, immune-synapse formation, migration, proliferation, and effector differentiation, while the mechanical properties of the extracellular environment influence how these signals are integrated [26–28]. Studies performed on two-dimensional substrates have shown that rigidity can regulate human T-cell activation and proliferation, whereas three-dimensional porous matrices have demonstrated that changes in stiffness may affect activation, cytokine production, motility, and cell division [29, 30]. Nevertheless, the relationship between matrix mechanics and T-cell behavior is not expected to be monotonic or universal. It depends on dimensionality, ligand availability, matrix architecture, confinement, cell activation state, and the timescale over which mechanical signals are applied. Consequently, any biological effect associated

with hydrogel stiffening should be interpreted as part of a broader mechanochemical and transport-dependent response rather than as the consequence of stiffness alone.

Dynamic culture offers a potential means of inducing such post-printing conditioning. Clinostat and rotating-wall-vessel systems were originally developed to reproduce selected aspects of microgravity, but they also function as low-shear suspension bioreactors capable of reducing sedimentation, maintaining three-dimensional droplets in continuous motion, and improving the exchange of nutrients, oxygen, and metabolites [31–35]. From a biofabrication perspective, their relevance therefore extends beyond altered gravity. Clinorotation reorganizes the hydrodynamic environment surrounding the droplet and exposes it to time-dependent fluid motion, residual droplet-medium slip, local velocity gradients, pressure variations, and cyclic changes in orientation. These effects may influence both mass transport and the internal organization of a flow-responsive hydrogel. Importantly, however, clinorotation should not be regarded as a simple or spatially uniform shear-stress stimulus. The effective mechanical loading experienced by a freely moving droplet depends on its trajectory, degree of co-rotation with the surrounding medium, distance from the chamber wall, and local flow field. The resulting condition is therefore more accurately described as flow-mediated hydrodynamic conditioning than as exposure to a single defined shear-stress value.

This distinction is also important when interpreting immune-cell responses. Real and simulated microgravity have produced heterogeneous and context-dependent effects on lymphocytes. Impaired activation and reduced IL-2-related signaling have been reported in primary T cells under several exposure conditions [36–39], whereas non-activated Jurkat cells have shown adaptive changes in morphology, metabolism, and proliferation that vary with exposure duration and experimental platform [40]. These observations argue against attributing cellular responses exclusively to gravity-vector averaging. In a cell-laden hydrogel droplet, clinorotation simultaneously modifies sedimentation, solute transport, waste clearance, matrix hydration, fluid-matrix interactions, and the mechanical state of the biomaterial. The biological outcome therefore reflects the integrated response of cells and matrix to a dynamically conditioned microenvironment.

In the present study, we investigated whether clinorotation could promote the flow-mediated mechanical conditioning of lymph node-inspired, Jurkat-laden droplets designed as a biophysical lymph node surrogate bioprinted from a nanocellulose-reinforced alginate bioink. Droplet trajectories and chamber hydrodynamics were characterized by video tracking and computational fluid dynamics, while local and bulk matrix mechanics were evaluated by atomic force microscopy nanoindentation and rheology. Alginate-only droplets were included to determine whether the mechanical response depended on the presence of the nanocellulose network. We then examined whether dynamic conditioning was associated with changes in Jurkat viability, proliferation, and metabolic activity. Finally, a simplified Jurkat/U87 transwell co-culture was used as a proof-of-concept system to evaluate the potential of dynamically matured droplets for immune-tumor interaction studies. Within this framework, the study addresses two interconnected questions: whether sustained hydrodynamic conditioning can reshape the mechanical state of a 3D-bioprinted nanocomposite hydrogel, and whether the resulting matrix and

transport environment can support improved expansion of Jurkat T cells. Because these variables are intrinsically coupled in the present experimental design, the observed biological effects are interpreted as the integrated consequence of flow-mediated matrix remodeling, dynamic mass transport, and suspension culture rather than as the isolated effect of shear stress or hydrogel stiffness. Additionally, Jurkat cells were selected as a reproducible and well-characterized surrogate for the biophysical component of this question; they do not reproduce the activation requirements, phenotypic heterogeneity, or receptor specificity of primary human T cells, and the present work is therefore positioned as a material- and process-level study.

2. Materials and methods

2.1. Cell Culture

Human glioblastoma cells (U87 MG) and human leukemic T-cell line Jurkat were obtained from the American Type Culture Collection (ATCC, Manassas, VA, USA). Cell lines were cultured in DMEM and RPMI 1640 medium (STEMCELL Technologies, Vancouver, BC, Canada), respectively, supplemented with 10% fetal bovine serum (FBS; EuroClone, Milan, Italy) and 1% penicillin-streptomycin (Sigma-Aldrich, St. Louis, MO, USA). Cells were maintained in T75 flasks (Corning Inc., NY, USA) at 37°C in a humidified atmosphere with 5% CO_2. Media were refreshed every 3 days, and cells were passaged upon reaching 80% confluence (U87) or a density of 2×10^6 cells/mL (Jurkat) to ensure logarithmic growth phase for all experiments.

2.2. Cell encapsulation and 3D bioprinting

To prepare the cell-laden bioink, Jurkat cells were pelleted and resuspended at a density of 10^7 cells/mL. This suspension was integrated into the CELLINK RGD nanocellulose-reinforced alginate (Alg/Cel/RGD) bioink (CELLINK, Boston, MA, USA) at a 1:10 v/v ratio. Homogeneous mixing was achieved using a sterile double-syringe system connected via a luer-lock adaptor. The resulting bioink was loaded into a 3 mL pneumatic cartridge and mounted on a BIO X6™ bioprinter (CELLINK). A droplet-based bioprinting strategy was employed, using an 18 G high-precision nozzle (inner diameter 840 μm) to dispense droplets into 24-well plates (Corning Inc.) of ~ 5 μm diameter. The printing parameters were set to an extrusion pressure of 10 kPa with an extrusion time of 2 s per droplet. Immediately after extrusion, the 3D-bioprinted models were chemically stabilized using a 5% (w/v) $CaCl_2$ ionic crosslinking solution for 5 minutes. Following crosslinking, the droplets were washed and incubated in fresh RPMI 1640 complete medium at 37°C with 5% CO_2.

The bioink was selected on the basis of a previous comparative study in which the nanoscale mechanical response of a panel of printable hydrogel formulations, including alginate, nanocellulose-reinforced RGD-functionalized alginate (CELLINK RGD), GelMA and modified GelMA-A, was characterized by AFM nanoindentation and bulk rheology [41]. Among the formulations tested, the nanocellulose-reinforced RGD-functionalized alginate exhibited apparent stiffness values closest to the range reported

for soft lymphoid tissue and was therefore selected for the present study. Three additional properties made this formulation suitable for the specific aims of this work. First, the fibrillar nanocellulose phase is responsive to hydrodynamic processing, and its orientation and packing can be modified by flow, which is a prerequisite for the post-printing mechanical maturation investigated here. Second, the RGD functionalization provides integrin-binding motifs that are absent from unmodified alginate and that support cell-matrix engagement within the construct. Third, the formulation is crosslinked ionically under mild conditions compatible with encapsulated lymphocytes and retains droplet shape fidelity at the extrusion parameters used, avoiding the photoinitiators and UV exposure required by methacrylated systems.

2.3 Excision of native murine lymph nodes

Axillary lymph nodes from *n* = 3 independent mice were collected upon sacrifice by carbon dioxide inhalation. Lymph nodes were identified in white-light stereomicroscopic examination and the surrounding connective tissue and fat were removed. The excised lymph nodes measured approximately 3.5 mm × 2.0 mm. Lymph nodes were kept in PBS and mechanical measurements were performed on the same day.

2.4. Clinostat culture and optimization of the hydrodynamic conditioning regime

The clinostat expansion of the 3D-bioprinted droplets was performed using the ClinoStar bioreactor system (CelVivo, Odense, Denmark). This system utilizes a rotating wall vessel (RWV) technology to create a low-shear environment, facilitating optimal nutrient exchange and high-density cell growth. A preliminary optimization phase was conducted to identify the ideal fluidic regime for the nanocellulose-reinforced droplets. Rotational speeds were systematically varied (ranging from 10 to 50 rpm) to evaluate their impact on droplet suspension and orbital stability. While lower speeds (≤ 15 rpm) maintained the droplets in a near-stationary state, they lacked sufficient mass transport. Conversely, higher speeds (> 45 rpm) introduced irregular trajectories and wall collisions. Based on the trajectory analysis performed via the SAM3 tracking pipeline (see Section 2.5), 25 rpm was selected as the standard operating speed for all subsequent experiments. At this velocity, the droplets followed a highly reproducible and stable circular orbit, effectively balancing the requirements for low shear stress with the need for a clean, consistent, and predictable motion path. All dynamic cultures were maintained at 37°C and 5% CO_2 within the ClinoStar climate-controlled chamber.

2.5. Deep learning pipeline for automated 3D droplet tracking

Videos of cells were analyzed in Python using a custom pipeline implemented in Google Colab on a A100 NVIDIA GPU. Video files were loaded with the transformers video utilities (OpenCV backend), and all frames were converted to PIL.Image format at their original spatial resolution. The frame rate and image dimensions were extracted from the video metadata to allow subsequent conversion from frame

index to physical time. Semi-automatic segmentation and tracking of individual cells were performed with the SAM3 Tracker Video model (Hugging Face Transformers). For each video, the first frame was displayed in an interactive widget, and the user manually annotated one or more positive point prompts on each cell of interest. These 2D point prompts were passed to the Sam3TrackerVideoProcessor, which initialized a video session and computed binary segmentation masks on the first frame for each labeled object. Masks were post-processed to the original image size and overlaid on the first frame to visually verify the correctness of the segmentation before tracking.

The validated prompts and object IDs were then used to initialize a full-video SAM3 tracking session. The model was run across all frames using the *propagate_in_video_iterator* interface, yielding a binary mask for each object and frame. For every frame and object, the droplet centroid was calculated as the mean of the mask pixel coordinates and stored as a trajectory point. To handle temporary tracking failures, trajectories were split into segments whenever gaps larger than one frame occurred. For visualization, colored masks, contours, cell labels, and polylines representing cumulative trajectories were rendered frame-by-frame on the original video using OpenCV, and the result was exported as an annotated MP4. Finally, all trajectories were exported to a CSV file using pandas. For each cell and trajectory segment, the CSV contained the object ID, segment ID, frame index, time in seconds (frame index divided by fps), and the centroid coordinates (x, y in pixels).

2.6. Computational fluid dynamics simulations

To characterize the hydrodynamic environment and quantify the mechanical stimuli acting on the bioprinted models, a computational fluid dynamics (CFD) simulation was performed using COMSOL Multiphysics software. The bioreactor geometry was modeled as a cylinder with a 30 mm radius, containing a fluid phase (density 1000 kg/m^3; dynamic viscosity 10^{-3} Pa·s). A rotating machinery physics interface with a moving mesh was implemented to simulate the specific operational rotational speeds. Slip wall boundary condition is used to model the effective non-ideal wall conditions that exist in the slip-flow regime. A time-dependent study was conducted with a total duration of 100 s and a time step of 1 s. The local shear stress was calculated using the product of dynamic viscosity and shear rate. Shear-stress profiles were extracted along the radial distance from the center of rotation to provide a quantitative map of the mechanical forces experienced by the bioprinted models.

2.7. AFM nanoindentation analysis

Nanoscale mechanical properties and matrix stiffening were characterized using a NanoWizard II AFM (JPK Instruments, Berlin, Germany). The system was equipped with high-resolution silicon probes (HQ:CSC37/No Al, MikroMasch) featuring a nominal spring constant of 0.3 N/m, a tip radius of 8 nm, and a 40° cone angle. This sharp geometry was selected to probe the nanocomposite at the nanoscale, enabling the detection of mechanical variations with high spatial resolution also in soft materials [42, 43]. Prior to each session, the cantilever spring constant was precisely determined via thermal calibration in distilled water. Indentation experiments were performed by approaching the sample surface at 10 µm/s, with a maximum force limit of 5.5 nN and an indentation depth of 5 µm. These

parameters were selected based on a previous optimization study performed on alginate and Alg/Cel/RGD hydrogels to reliably capture their viscoelastic response [41].

To maintain physiological-like conditions and prevent dehydration, all measurements were conducted in distilled water within a controlled environment. For both the experimental conditions (bioprinted droplets in static culture vs. clinostat culture), a total of 64 force-distance curves were acquired over a 10×10 μm^2 grid. A total of three maps were collected at randomly selected positions on each droplet, and three independently bioprinted and cultured droplets were analyzed per condition. The apparent Young's modulus was calculated using JPK Data Processing software (version 6.1) by fitting the approach curve with the Hertz-Sneddon model for a conical indenter [44, 45]. In accordance with established literature for alginate-based hydrogels and soft biomaterials, a Poisson's ratio of 0.33 was assumed [41]. This assumption is consistent with previous reports on alginate-based hydrogels, which typically exhibit Poisson's ratios in the range of 0.2–0.4 [46–49].

2.8. Rheological characterization

The bulk viscoelastic properties of the bioprinted droplets were evaluated using a Haake MARS 60 controlled-stress rheometer (Thermo Fisher Scientific, Karlsruhe, Germany) equipped with 8 mm and 25 mm diameter parallel plate-plate configurations. Prior to each measurement, the samples were equilibrated at 25°C to ensure thermal stability. To identify the linear viscoelastic region (LVR), amplitude sweep tests were initially performed at a constant oscillation frequency of 1 Hz, with the strain γ ranging from 0.001 to 10. Frequency sweep tests were conducted within a range of 0.01 to 10 Hz under oscillatory mode at a constant strain determined from the LVR results (γ = 0.02 for both alginate and Alg/Cel/RGD) to ensure non-destructive testing conditions. The storage modulus G' and loss modulus G'' were recorded as a function of frequency to quantify the macroscopic stiffness and the structural integrity of the nanocellulose-reinforced network.

2.9. Cell viability and cytotoxicity

The viability of encapsulated Jurkat cells was monitored over 10 days at specific time points (days 0, 1, 5, and 10) using a Live/Dead fluorescence assay. Briefly, Calcein-AM (Invitrogen, Carlsbad, CA, USA) and propidium iodide (PI) (Sigma-Aldrich) were subsequently added to the culture medium at a final concentration of 1 µM and 5 µM to label live and dead cells, respectively. Following 25 minutes (calcein) and 7 min (PI) of incubation at 37°C, fluorescence images and intensities were acquired using a Cytation™ 3 Cell Imaging Multi-Mode Reader (BioTek Instruments, Winooski, VT, USA). To evaluate potential matrix-induced toxicity, lactate dehydrogenase (LDH) production was measured in the culture supernatants using a commercial LDH assay kit (Roche, Basel, Switzerland). Supernatants were collected and diluted before incubation with the reaction substrate. After 30 minutes, absorbance was recorded at 490 nm and 680 nm using the Cytation™ 3 reader.

2.10. Proliferation and metabolic activity assays

To evaluate the expansion efficiency within the 3D-bioprinted droplets, we evaluated intracellular ATP production, protein release, and DNA synthesis. Specifically, cell viability and metabolic activity were assessed using the CellTiter-Glo 3D Luminescent Assay (Promega, Madison, WI, USA). At days 1, 4, 7, and 10, the droplets were rinsed with PBS and incubated with CellTiter-Glo 3D reagent and culture medium in the ratio 1:1. The models were agitated for 5 minutes to ensure complete cell lysis and then incubated for 25 min at room temperature in the dark to stabilize the signal. Luminescence was recorded using the Cytation 3 reader.

Total protein concentration was quantified using the Bicinchoninic Acid (BCA) Protein Assay Kit (Thermo Fisher Scientific, Waltham, MA, USA). Prior to the assay samples were centrifuged to discard potential debris from supernatants. Then 10 µL of each sample supernatants was placed into a 96-multiwell plate, followed by adding 200 µL of BCA Protein Assay reagent. The multiwell was incubated at 37°C for 30 min and then mixed on a plate shaker. The absorbance of each sample, blank, and standard was measured with the Cytation 3 reader at 560 nm.

Active cellular proliferation was confirmed by labeling newly synthesized DNA with 5-Ethynyl-2-deoxyuridine (EdU) using Click-iT™ EdU Cell Proliferation Kit (Thermo Fisher Scientific, Waltham, MA, USA). A volume of 10 µM EdU was incorporated into the culture medium to identify the population of cells undergoing active division during the expansion period. Following a 24 h incubation period, EdU incorporation was quantified. This was performed by introducing the Amplex UltraRed reagent to obtain a highly fluorescent product at room temperature for 15 min. Fluorescence intensity was recorded at excitation/emission wavelengths of 560/590 nm using Cytation 3 reader.

2.11. Jurkat/U87 transwell co-culture assay

To assess whether Jurkat cells expanded within 3D-bioprinted droplets could be used in a simplified immune-tumor interaction model, a proof-of-concept transwell co-culture assay was established with U87 glioblastoma cells. U87 cells were seeded in 24-well plates at a density of 5×10^4 cells per well. Jurkat-laden 3D-bioprinted droplets, previously cultured for 10 days under either static or clinostat conditions, were then transferred into transwell inserts with an 8 µm pore-size membrane (Corning Inc.). The inserts were positioned above the U87 monolayer to allow soluble-factor exchange and Jurkat cell release and transmigration through the membrane toward the lower compartment. As an additional control, non-encapsulated Jurkat cells were added to separate transwell inserts.

The co-culture was monitored over 48 h to evaluate the response of the U87 glioblastoma cells to the different Jurkat conditioning. U87 viability and cell death were assessed by calcein/PI staining, respectively, as described in Section 2.9. To identify U87 cell death, apoptosis/necrosis was evaluated by Annexin V/PI staining with Vybrant Apoptosis Assay Kit. Briefly, U87 glioblastoma cells were rinsed and incubated with 100 µL 1× annexin-binding buffer. Next, 5 µL of biotin-X annexin V was added and incubated for 15 min at room temperature. Samples were washed and stained with 1 µL of 1 mg/mL Alexa Fluor 350 streptavidin solution, followed by a 30-minute incubation. After rinsing, 1 µL of 1 mg/mL PI was added and incubated for 6 min at room temperature. Fluorescence intensity was recorded at

excitation/emission wavelengths of 365/440 nm (Alexa Fluor 350) and 535/617 nm (PI), using Cytation 3 reader.

Oxidative stress responses were investigated by measuring intracellular reactive oxygen species (ROS) (CellROX, Life Technologies, Carlsbad, CA, USA) and extracellular ROS (ROS-ID, Enzo Life Sciences, Farmingdale, NY, USA) levels in U87 cell culture and cell supernatants, respectively. Intracellular and extracellular ROS were evaluated at 0, 24, 48 h. For intracellular ROS evaluation, cells were stained with CellROX Reagent at 5 μM concentration and incubated with cells for 30 minutes at 37°C. Cells were then rinsed with PBS and fluorescence intensity was recorded at excitation/emission wavelengths of 485/520 nm using Cytation 3 reader. For extracellular ROS evaluation, Oxidative Stress Detection Reagent was gently mixed with cell supernatants to obtain a 1:2500 diluted staining solution. Fluorescence intensity was recorded at excitation/emission wavelengths of 490/525 nm using Cytation 3 reader.

2.12 Multiplex cytokine profiling

Cytokine levels TNF-α, IFN-γ, IL-1β, IL-6, IL-8/CXCL8, and IL-10 were quantified in culture supernatants collected during the Jurkat/U87 transwell co-culture assay using a Luminex bead-based multiplex immunoassay. Supernatants were collected at 0, 24, and 48 h from both the lower and upper transwell compartments. The lower chamber contained the U87 monolayer and Jurkat cells released from the droplets and migrated through the 8 μm membrane, whereas the upper chamber contained the Jurkat-laden 3D-bioprinted droplet. Immediately after collection, supernatants were centrifuged at 16,000 g for 4 min to remove cells and debris. Standard curve dilutions and samples were then added to a 96-well assay plate at a volume of 50 μL per well. Subsequently, 50 μL of Microparticle Cocktail was added to each well, and the plate was incubated overnight at 4°C under agitation at 800 rpm. For each washing step, the plate was placed on a magnetic separator for 2 min to allow magnetic bead immobilization, after which the supernatant was carefully removed. Wells were washed three times with 100 μL of wash buffer.

After the overnight incubation and washing steps, 50 μL of Biotin-Antibody Cocktail was added to each well and incubated for 1 h at room temperature under agitation at 800 rpm. The plate was then washed three times as described above. Subsequently, 50 μL of Streptavidin-PE solution was added to each well and incubated for 30 min at room temperature under agitation at 800 rpm. After three additional washes, the magnetic beads were resuspended in 100 μL of wash buffer and incubated for 2 min at room temperature under agitation at 800 rpm. The plate was read immediately using a Bio-Plex 200 system. Cytokine concentrations were calculated from the corresponding standard curves and expressed as concentration values for each analyte.

2.13. Statistical analysis

All experimental data were obtained from at least three independent replicates, and results are expressed as mean value ± standard deviation (SD). Statistical significance was evaluated using one-way or two-way analysis of variance (ANOVA), followed by Tukey’s post-hoc tests for multiple comparisons, depending on the experimental design and the number of variables (e.g., comparing different time

points, hydrogel compositions, or culture conditions). For the comparison between two specific groups at a single time point, a two-tailed Student's t-test was used. The thresholds for statistical significance were defined as follows: * $p < 0.05$, ** $p < 0.01$, *** $p < 0.001$, **** $p < 0.0001$. All statistical computations and data visualization were realized on GraphPad Prism (version 10.4.0). Differences with a *p*-value > 0.05 were considered not statistically significant (*ns*).

3. Results and discussion

3.1. Clinorotation establishes a stable low-shear hydrodynamic regime

Clinostat technology imposes a hydrodynamic condition that differs fundamentally from a conventional stirred or perfused bioreactor. In this system, the culture chambers are continuously rotated to average the gravity vector over time and maintain 3D droplets in a suspension-based low-shear state (Fig. 1a,b). Therefore, the bioprinted droplets act as freely moving bodies whose trajectories result from the balance between gravity force, buoyancy, hydrodynamic drag, lift, and centripetal components generated by local velocity and pressure gradients (Fig. 1c).

To identify the operating regime as a function of the angular velocity, videos of droplet motion were analyzed using a SAM3-based tracking pipeline, which enabled segmentation of the droplet contour and reconstruction of its trajectory at increasing rotational speeds (Fig. 1d). At 15 rpm, droplets exhibited negligible displacement and remained confined to small trajectories, indicating limited averaging of the gravity vector. Increasing the rotational speed to 25–35 rpm generated stable, reproducible orbital trajectories with progressively larger radii 8–13 mm. This intermediate regime is consistent with controlled clinorotation, in which the droplets remain suspended and cyclically advected by the surrounding medium without evident wall collisions. At 45 rpm, the orbital radius increased to 20 mm and the droplets approached the chamber periphery, reducing wall clearance and increasing the probability of intermittent wall contact. Above this range, droplet motion became irregular and was associated with collisions between droplets and against the chamber wall, leading to visible matrix damage and fragmentation. These unstable and collisional conditions were therefore excluded from subsequent experiments.

CFD simulations were used to map the hydrodynamic environment of the rotating chamber in the absence of the constructs (Fig. 1e,f). The simulated field therefore describes the chamber-frame fluid stress and corresponds to the shear stress that a droplet would experience only in the limiting case in which it remained stationary relative to the surrounding medium. This condition is approached at low rotational speeds, where trajectory analysis showed negligible droplet displacement (15 rpm), and the simulated values would represent an overestimate of the stress acting on the droplets. At the operating speed of 25 rpm, the droplets followed stable orbital trajectories and largely co-rotated with the medium, so that the effective hydrodynamic stress is governed by the residual droplet-medium slip and is expected to be substantially lower than the simulated values.

3.2. Clinorotation-associated stiffening of nanocellulose-alginate droplets

The identification of a stable low-shear orbital regime raised the question of whether prolonged clinorotation could modify the mechanical state of the printed hydrogels. This aspect is critical for the present platform, since the clinostat condition simultaneously alters droplet suspension, fluid redistribution, and medium exchange. Therefore, the mechanical response was evaluated at both the local and bulk scales, and compared between the nanocellulose-reinforced alginate and alginate hydrogels. At the macroscopic level, Alg/Cel/RGD droplets recovered after clinostat culture appeared more compact and more opaque than static controls (Fig. 2a). This suggests that clinorotation may promote post-printing matrix maturation, possibly through a combination of fluid redistribution, continued ionic equilibration, and reorganization of the fibrillar nanocellulose-containing network.

AFM nanoindentation was first used to assess whether clinostat culture altered the local mechanical response of Alg/Cel/RGD droplets and whether the resulting stiffness approached that of native lymphoid tissue in murine model. Force-indentation curves showed a larger loading response in clinostat-cultured droplets compared with static samples, indicating increased resistance to local deformation (Fig. 2b). Quantification of the apparent Young's modulus confirmed this trend, with clinostat-cultured droplets displaying an approximately 5-fold increase in local stiffness relative to static controls (Fig. 2c). Importantly, native murine axillary lymph nodes were included as a biological mechanical reference. The stiffness values measured in clinostat-cultured Alg/Cel/RGD droplets shifted toward the range observed in axillary lymph nodes, suggesting that clinostat conditioning brings the printed hydrogel closer to a lymphoid-tissue-like mechanical regime.

Bulk rheology was then performed to determine whether the local stiffening detected by AFM was reflected in the macroscopic viscoelastic behavior of the hydrogels and whether this response depended on the presence of nanocellulose. Native murine axillary lymph nodes were included as a bulk tissue reference to contextualize the viscoelastic range of the printed matrices under physiologically relevant conditions. In Alg/Cel/RGD hydrogels, oscillatory amplitude sweeps revealed higher storage modulus values after clinostat culture together with a stronger elastic response within the low-strain region before strain-induced yielding (Fig. 3a). Frequency sweeps confirmed this trend, with clinostat cultured Alg/Cel/RGD samples maintaining higher storage modulus values over the tested frequency range (Fig. 3b). Notably, the bulk viscoelastic response of clinostat-cultured Alg/Cel/RGD droplets shifted toward the range measured in native murine axillary lymph nodes, suggesting that dynamic conditioning promotes a more lymphoid-tissue-like mechanical behavior at the macroscopic scale (Fig. 3i-l). The corresponding loss modulus measurements showed that the dissipative component also changed with culture time and condition (Fig. 3c,d), but the storage modulus remained dominant over most of the tested range, supporting the persistence of a solid-like hydrogel network.

In contrast, alginate droplets exhibited opposite behavior. Specifically, in both amplitude and frequency sweeps, the most pronounced mechanical reinforcement was observed under static culture, whereas

clinostat cultured alginate hydrogels showed only minor changes in storage modulus over time indicating that dynamic low-shear culture is not sufficient to induce marked stiffening in the absence of nanocellulose fibers (Fig. 3e,f). This suggests that alginate droplets mainly undergo time-dependent static maturation, likely related to ongoing ionic equilibration and network relaxation. Interestingly, the concomitant increase in G'' suggests that static alginate maturation involved enhanced viscous dissipation within the ionically crosslinked network (Fig. 3g,h).

3.3. Clinostat culture enhances Jurkat T-cell viability, proliferation, and metabolism

The formulation-dependent stiffening observed in Alg/Cel/RGD droplets prompted us to investigate whether clinostat culture and concurrent mechanical changes were associated with improved Jurkat cell maintenance and growth within the 3D-bioprinted droplet. Static and clinostat cultured droplets were therefore compared using complementary assays of cell viability, membrane damage, DNA synthesis, intracellular ATP content, and total protein accumulation. These assays report distinct cellular properties, namely esterase activity and membrane integrity (calcein/PI), membrane damage (LDH), the fraction of cells in S phase during a short labelling pulse (EdU), intracellular ATP content, and total protein accumulation. None of them provides an absolute measurement of cell number, and the corresponding fold changes are used here as concordant, qualitative indicators of the relative culture performance of the two conditions. We emphasize that matrix stiffening is not proposed here as the causal driver of the improved Jurkat expansion. Clinorotation concurrently modifies matrix mechanics, oxygen and nutrient transport, metabolite clearance, sedimentation, and fluid-matrix interaction, and the present design cannot separate these contributions.

Representative Live/Dead imaging showed distinct differences between the two culture conditions (Fig. 4a). Static droplets contained viable Jurkat cells but also exhibited a more pronounced PI-positive signal, consistent with the accumulation of dead or membrane-compromised cells within the confined 3D matrix. In contrast, clinostat cultured droplets showed a stronger calcein-positive signal and a lower relative PI signal, suggesting improved preservation of cell viability during culture. Calcein fluorescence increased over time in both conditions, indicating that the bioprinted cell-laden Alg/Cel/RGD matrix was permissive to Jurkat cell maintenance and growth (Fig. 4b). However, clinostat cultured droplets showed 1.4 times higher calcein signal at day 10 compared to static control. PI fluorescence also increased during culture, as expected in a high-density 3D system where cell accumulation and local crowding can lead to progressive cell death. However, this increase was much more pronounced under static culture than under clinostat condition (Fig. 4c).

LDH release provided an additional measure of compromised cell membrane. Static droplets showed a progressive increase in LDH signal over time, whereas clinostat cultured droplets maintained lower LDH levels throughout the culture period (Fig. 4d). This reduction in LDH release is consistent with the low-shear suspension regime improving the local culture environment, likely by reducing nutrient and oxygen depletion zones and facilitating removal of metabolic waste. Proliferative activity, assessed by EdU

incorporation, further supported this interpretation. Although both conditions supported DNA synthesis, clinostat cultured droplets exhibited higher EdU signal with a 1.6-fold enhancement at day 10 (Fig. 4e). The strongest difference between static and clinostat culture was observed in the ATP and total protein levels. CellTiter-Glo 3D assay showed a marked 5-fold increase in intracellular ATP level in clinostat cultured droplets at day 10 (Fig. 4f). Since intracellular ATP reflects both the number of viable cells and their metabolic state, this value cannot be converted into a cell number and is reported here as a combined indicator of viable, metabolically active cell content. Consistently, BCA analysis revealed greater total protein accumulation up to 2.3-fold in the clinostat group compared with static controls (Fig. 4g), further supporting increased biomass formation within the dynamically cultured droplets.

3.4. Culture and delivery conditions of Jurkat-laden droplets differentially affect U87 responses in a transwell co-culture model

To determine whether the preceding culture and delivery conditions influenced the response of a heterotypic tumor-cell culture, Jurkat-laden droplets were co-cultured with U87 glioblastoma cells in a transwell model. The comparison was performed between delivery formats as a whole, that is, between the entire constructs as they are generated by each culture protocol, and the groups were deliberately not normalized to an equal number of viable Jurkat cells. This design reflects the intended use of the platform, in which the construct rather than the isolated cell is the functional unit, but it also implies that the resulting differences integrate cell abundance, metabolic state, migration, and secreted factors, which the present experiment cannot separate.

U87 cells were seeded in the lower chamber, whereas Jurkat cells were introduced into the upper compartment in three different formats: as free suspension cells, within droplets previously maintained under static culture for 10 days, or within droplets previously expanded under clinorotation for 10 days (Fig. 5a). The 8 μm porous membrane allowed soluble-factor exchange and potential Jurkat migration toward the U87 monolayer, thereby enabling comparison of the effects associated with the different Jurkat culture and delivery conditions. Live/Dead fluorescence imaging revealed distinct changes in the U87 compartment over the 48-hour co-culture period (Fig. 5b). In control cultures, calcein fluorescence progressively increased, consistently with continued U87 growth. Free Jurkat cells and Jurkat-laden droplets maintained under static conditions attenuated this increase but did not produce a clear net reduction in the calcein-positive U87 area. In contrast, droplets previously cultured under clinorotation produced a marked suppression of U87 growth, with an approximately 60% reduction in the calcein-positive signal after 48 hours (Fig. 5c,e). This response was accompanied by an approximately 8-fold increase in PI fluorescence (Fig. 5d), indicating a substantial increase in membrane-compromised and dead cells within the lower compartment. Thus, the reduced calcein-positive area observed in the clinostat condition (Fig. 5b) was associated not only with limited U87 expansion but also with increased cell damage and death.

Apoptosis-associated staining further supported this response. Although an increase was observed in all co-culture conditions, the apoptosis-associated fluorescence signal was approximately 2.6-fold higher in

U87 cultures exposed to clinostat-expanded droplets than in those exposed to free Jurkat cells and static droplets (Fig. 5f). These results indicate that the stronger suppression of U87 growth in the clinostat condition was accompanied by a more pronounced cell death-associated response. Oxidative stress-related measurements showed a similar condition-dependent pattern. Intracellular ROS levels progressively decreased in U87 control cultures, whereas free Jurkat cells and static Jurkat-laden droplets induced only moderate or transient changes. In contrast, exposure to clinostat-expanded droplets resulted in a progressive increase in intracellular ROS over 48 hours (Fig. 5g). Extracellular ROS also increased, reaching approximately 2.2-fold relative to the initial value in the clinostat condition (Fig. 5h). These measurements demonstrate the establishment of a stronger oxidative environment during co-culture with clinostat-expanded droplets. However, extracellular ROS may originate from stressed or dying U87 cells, migrated Jurkat cells, or reciprocal interactions between the two cell populations. The ROS measurements should therefore be regarded as integrated indicators of oxidative stress within the co-culture system rather than as evidence of a specific cellular mechanism.

The greater effect produced by clinostat-cultured droplets is likely influenced, at least in part, by the higher viable Jurkat biomass generated during the preceding 10-day dynamic culture. As shown in Fig. 4, clinorotation was associated with higher Jurkat viability, EdU incorporation, intracellular ATP, and total protein accumulation. Consequently, a larger number of viable and metabolically active Jurkat cells may have been available for release, migration, and soluble-factor production during the subsequent interaction with U87 cells. Because the groups were not normalized to the same number of viable Jurkat cells at the beginning of the co-culture and the number of cells migrating through the transwell membrane was not independently quantified, the relative contributions of cell abundance, migration, metabolic state, and secreted factors cannot be separated in the present experimental design. Multiplex cytokine profiling was subsequently performed to characterize the soluble environment associated with the different culture conditions (Fig. 6). Control Jurkat and U87 cultures displayed distinct basal cytokine profiles in the upper and lower compartments, respectively (Fig. 6a,b). U87 controls showed a profile dominated by IL-8/CXCL8, IL-6, and TNF-α. This pattern is consistent with the inflammatory and pro-angiogenic secretory phenotype described for glioblastoma cells. In particular, IL-8/CXCL8 has been associated with neutrophil recruitment, angiogenesis, and glioblastoma progression [50, 51], whereas IL-6 and TNF-α are involved in inflammatory signaling pathways that can support tumor survival, invasion, immune escape, and treatment resistance [52–54].

In the upper compartment, Jurkat-laden droplets produced a distinct cytokine profile characterized by a prominent IL-10 signal, which was more pronounced after clinostat culture (Fig. 6c,e). IL-10 is a context-dependent immunoregulatory cytokine whose biological effects vary according to the producing cell population and the surrounding cytokine environment [55]. Therefore, its increase identifies a modification of the soluble profile associated with dynamic culture but cannot, in the absence of direct phenotypic and functional measurements, be considered evidence of Jurkat activation or enhanced cytotoxic competence. In the lower compartment, increased IL-6 and TNF-α levels were detected during Jurkat/U87 co-culture, with the highest concentrations observed following exposure to clinostat-expanded droplets (Fig. 6d,f). IFN-γ remained comparatively low, although a moderate increase was

observed in the clinostat condition. Since cytokines collected from the lower chamber may originate from U87 cells, migrated Jurkat cells, or both populations, their cellular source cannot be assigned from the present measurements. Similarly, although IL-10 has been reported to modulate IFN-γ-associated responses in other experimental systems [56, 57], the present data do not establish a direct causal relationship between these cytokines. Therefore, the multiplex cytokine analysis demonstrates that the Jurkat expansion and delivery conditions were associated with distinct changes in the soluble inflammatory environment of the co-culture.

These results show that Jurkat-laden droplets previously expanded under clinorotation produced a stronger effect on the U87 co-culture than static droplets or free Jurkat controls. This effect was characterized by reduced U87 growth, increased membrane damage and apoptosis-associated signals, enhanced oxidative stress, and a modified cytokine profile. The response is likely influenced by the greater viable Jurkat biomass generated during dynamic culture and should not be interpreted as evidence of antigen-specific recognition or cytotoxic cell activity, since Jurkat cells are an immortalized leukemia-derived cell line and were not specifically directed against U87 cells. Nevertheless, the experiment provides a functional proof of concept showing that Jurkat cells expanded within dynamically conditioned droplets remain capable of substantially modifying the behavior and soluble environment of a heterotypic tumor-cell co-culture.

4. Conclusions

In this study, we developed a lymph node-inspired 3D-bioprinted platform based on a nanocellulose-reinforced alginate bioink and demonstrated that clinorotation can act as a flow-mediated post-printing conditioning strategy. Trajectory tracking and computational fluid dynamics identified a stable low-shear hydrodynamic regime in which the droplets remained suspended and followed reproducible orbital trajectories. Exposure to this dynamic environment induced pronounced mechanical maturation of the nanocellulose-alginate droplets, as demonstrated by the marked increase in apparent Young's modulus measured by AFM nanoindentation and by the enhancement of the elastic response observed through bulk rheology.

The mechanical response was strongly dependent on hydrogel composition. Whereas nanocellulose-reinforced droplets underwent substantial stiffening during dynamic culture, alginate-only hydrogels exhibited predominantly time-dependent maturation under static conditions and showed limited reinforcement under clinorotation. This differential behavior identifies the nanocellulose fibrillar network as a critical determinant of the hydrogel response to hydrodynamic conditioning and supports the concept that selected nanocomposite bioinks remain mechanically evolvable after printing.

Flow-mediated conditioning was accompanied by improved performance of the Jurkat-laden droplets, including higher cell viability, reduced LDH release, enhanced proliferation, and increased intracellular ATP and total protein accumulation compared with static culture. These findings indicate that dynamic culture generated a more permissive environment for the growth of encapsulated Jurkat T cells within

the 3D-bioprinted matrix. Nevertheless, the present experimental design does not permit the biological contribution of matrix stiffening to be separated from the concurrent effects of enhanced nutrient and oxygen transport, reduced sedimentation, improved waste removal, and altered fluid-matrix interactions. The observed cellular response should therefore be interpreted as the integrated outcome of mechanical matrix maturation and dynamic mass transport rather than as the isolated consequence of shear stress or stiffness.

As proof of concept, dynamically conditioned Jurkat-laden droplets were subsequently interfaced with U87 glioblastoma cells in a transwell co-culture model. Droplets previously maintained under clinorotation produced a greater reduction in U87 viability and were associated with increased apoptosis-related and oxidative stress signals compared with static droplets and free-cell controls. This effect is likely influenced by the greater viable Jurkat biomass generated during dynamic expansion and cannot be considered evidence of antigen-specific antitumor activity. Moreover, Jurkat cells are an immortalized leukemia-derived T-cell line and do not recapitulate the phenotypic heterogeneity, activation state, receptor specificity, or functional competence of primary human lymphocytes. The Jurkat/U87 system should therefore be regarded as a simplified interaction model rather than as a therapeutic validation.

Future studies should determine whether the mechanical and biological effects observed here extend to primary human T cells and PBMCs, which differ in activation requirements, mechanosensitivity, and metabolic profile, and whose validation is a necessary step before any translational claim can be made. Experimental designs that independently modulate matrix stiffness, hydrodynamic loading, and mass transport will also be required to resolve their respective contributions. Further development of the platform should incorporate more representative lymphoid components, controlled biochemical stimulation, and direct assessment of immune-cell phenotype, cytokine production, migration, and cytotoxic function.

Declarations

Ethical Approval

Animal studies were approved by the Italian Ministry of Health (permit no. 566/2024-PR) and conducted in accordance with institutional guidelines.

Clinical trial number

Not applicable.

Consent to Participate

declaration

Declaration of competing interest

The authors declare that they have no known competing financial interests or personal relationships that could have appeared to influence the work reported in this paper.

Funding

This work was supported by Catholic University of Sacred Hearth research funds.

Author Contribution

A.M. contributed to the conceptualization, experimental design, investigation, data analysis, visualization, and writing of the original manuscript draft. D.E. and M.M. contributed to experimental investigation, data acquisition, data analysis, and writing of the original manuscript draft. G.Pe. contributed to conceptualization, methodology, data interpretation, and manuscript review and editing. G.DG. and G.A. contributed to experimental investigation, data collection, and validation. V.P. contributed to methodology, data analysis, and critical revision of the manuscript. G.Pi. and C.C. contributed to biological investigations, murine lymph node excision, data interpretation, and manuscript review and editing. M.DS. contributed to scientific supervision, data interpretation, and critical revision of the manuscript. M.P. contributed to conceptualization, scientific supervision, and manuscript review and editing. All authors read and approved the final manuscript and agree to be accountable for their respective contributions and for ensuring that questions concerning the accuracy or integrity of the work are appropriately addressed.

Acknowledgement

We would like to acknowledge the contribution of 3D-Bioprinting Core Facility G-STeP of the Fondazione Policlinico Universitario “A. Gemelli” IRCCS for sample processing and the contribution of Microscopy Core Facility G-STeP of the Fondazione Policlinico Universitario “A. Gemelli” IRCCS for sample imaging. The publication of this article was financially supported by Università Cattolica del Sacro Cuore (Linea D3.1).

Data Availability

All the data presented in the study are available from the corresponding authors on reasonable request.

References

1. Chen S, Nguyen TD, Lee K-Z, Liu. D 2024 Ex vivo T cell differentiation in adoptive immunotherapy manufacturing: Critical process parameters and analytical technologies. Biotechnol Adv 77 108434.
2. Cheung AS, Zhang DK, Y, Koshy ST, Mooney DJ. Scaffolds that mimic antigen-presenting cells enable ex vivo expansion of primary T cells. Nat Biotechnol. 2018;36:160–9.
3. Zhang H, Liu F, Zhao J, Wang Y, Shen Y, Li Q, Luo H, Chen Y, Li R, Zhu. F 2025 Biomimetic lymph node-like scaffolds for optimized CAR-T cell expansion and potentiated antitumor efficacy. J Mater Chem B 13 11708–21.
4. Kim HS, Ho T-C, Willner MJ, Becker MW, Kim H-W, Leong. K W 2023 Dendritic cell-mimicking scaffolds for ex vivo T cell expansion. Bioact Mater 21 241–52.
5. Pandit S, Smith BE, Birnbaum ME, Brudno. Y 2024 A biomaterial platform for T cell-specific gene delivery. Acta Biomater 177 157–64.
6. Xie R, Pal V, Yu Y, Lu X, Gao M, Liang S, Huang M. Peng W and Ozbolat I T 2024 A comprehensive review on 3D tissue models: Biofabrication technologies and preclinical applications *Biomaterials* 304 122408.
7. Unagolla JM, Jayasuriya AC. Hydrogel-based 3D bioprinting: A comprehensive review on cell-laden hydrogels, bioink formulations, and future perspectives. Appl Mater Today. 2020;18:100479.
8. Mazzaglia C, Shery Huang YY, Shields JD. Advancing tumor microenvironment and lymphoid tissue research through 3D bioprinting and biofabrication. Adv Drug Deliv Rev. 2025;217:115485.
9. Mu P, Zhou S, Lv T, Xia F, Shen L, Wan J, Wang Y, Zhang H, Cai S, Peng. J 2023 Newly developed 3D in vitro models to study tumor–immune interaction. J Experimental Clin Cancer Res 42 81.
10. Minopoli A, Perini G, Cui L, Palmieri V, De Spirito M, Papi M. Biomaterial-driven 3D scaffolds for immune cell expansion toward personalized immunotherapy. Acta Biomater. 2025;200:132–57.
11. Cai Z, Lin K, Dong X, Li Z, Chen G, Guo L, Mou P, Chen P, Huang J, Li. L 2025 Implantable artificial lymph node enables rapid in vivo neoantigen-specific T-cell generation and expansion for improving antitumor immunity. J Immunother Cancer 13 e013043.
12. Kim D, Jo S, Lee D, Kim SM, Seok JM, Yeo SJ, Lee JH, Lee JJ, Lee K, Kim TD, Park S. A 2023 NK cells encapsulated in micro/macropore-forming hydrogels via 3D bioprinting for tumor immunotherapy. Biomater Res 27 60.
13. Liu B, Jin M, Ma C, Zhang Z, Ma L, Zhang Y, Wang D-A. 2024 An engineered lymph node comprising porous collagen scaffold with hybridized biological signals embedded in B cell membrane coatings *Biomaterials* 304 122420.
14. Liao Z, Jiang J, Wu W, Shi J, Wang Y, Yao Y, Sheng T, Liu F, Liu W, Zhao. P 2024 Lymph node-biomimetic scaffold boosts CAR-T therapy against solid tumor. Natl Sci Rev 11 nwae018.
15. Cui H, Zhao Y-Y, Han Y-H, Lan Z, Zou K-L, Cheng G-W, Chen H, Zhong P-L, Chen Y, Ma L-M, Chen T-K, Yu G-T. Lymph node targeting strategy using a hydrogel sustained-release system to load effector memory T cells improves the anti-tumor efficacy of anti-PD-1. Acta Biomater. 2024;180:423–35.

16. Markstedt K, Mantas A, Tournier I, Martínez Ávila H, Hagg D, Gatenholm. P 2015 3D bioprinting human chondrocytes with nanocellulose–alginate bioink for cartilage tissue engineering applications *Biomacromolecules* 16 1489–96.
17. Nguyen D, Hägg DA, Forsman A, Ekholm J, Nimkingratana P, Brantsing C, Kalogeropoulos T, Zaunz S, Concaro S, Brittberg. M 2017 Cartilage tissue engineering by the 3D bioprinting of iPS cells in a nanocellulose/alginate bioink. Sci Rep 7 658.
18. Aarstad O, Heggset EB, Pedersen IS, Bjørnøy SH, Syverud K, Strand BL. 2017 Mechanical properties of composite hydrogels of alginate and cellulose nanofibrils. Polym (Basel). 9378.
19. Cai Y, Chang SY, Gan SW, Ma S, Lu WF. and Yen C-C 2022 Nanocomposite bioinks for 3D bioprinting. Acta Biomater 151 45–69.
20. Bonilla MR, Lopez-Sanchez P, Gidley MJ, Stokes JR. Micromechanical model of biphasic biomaterials with internal adhesion: Application to nanocellulose hydrogel composites. Acta Biomater. 2016;29:149–60.
21. Mohammadi P, Toivonen MS, Ikkala O, Wagermaier W, Linder MB. Aligning cellulose nanofibril dispersions for tougher fibers. Sci Rep. 2017;7:11860.
22. Håkansson KMO, Fall AB, Lundell F, Yu S, Krywka C, Roth SV, Santoro G, Kvick M. Prahl Wittberg L and Wågberg L 2014 Hydrodynamic alignment and assembly of nanofibrils resulting in strong cellulose filaments. Nat Commun 5 4018.
23. Hoogenkamp HR, Bakker G-J, Wolf L, Suurs P, Dunnewind B, Barbut S, Friedl P, van Kuppevelt TH, Daamen. W F 2015 Directing collagen fibers using counter-rotating cone extrusion. Acta Biomater 12 113–21.
24. Rossy J, Laufer JM, Legler DF. 2018 Role of Mechanotransduction and Tension in T Cell Function. Front Immunol 9.
25. Wahl A, Dinet C, Dillard P, Nassereddine A, Puech P-H, Limozin L, Sengupta. K 2019 Biphasic mechanosensitivity of T cell receptor-mediated spreading of lymphocytes *Proceedings of the National Academy of Sciences* 116 5908–13.
26. Majedi FS, Hasani-Sadrabadi MM, Thauland TJ, Li S, Bouchard LS, Butte MJ. 2020 T-cell activation is modulated by the 3D mechanical microenvironment *Biomaterials* 252 120058.
27. Judokusumo E, Tabdanov E, Kumari S, Dustin ML, Kam LC. 2012 Mechanosensing in T lymphocyte activation. Biophys J 102 L5–7.
28. Rushdi M, Li K, Yuan Z, Travaglino S, Grakoui A, Zhu. C 2020 Mechanotransduction in T cell development, differentiation and function *Cells* 9 364.
29. O'Connor RS, Hao X, Shen K, Bashour K, Akimova T, Hancock WW, Kam LC, Milone MC. 2012 Substrate Rigidity Regulates Human T Cell Activation and Proliferation. J Immunol 189 1330–9.
30. Yuan DJ, Shi L, Kam LC. 2021 Biphasic response of T cell activation to substrate stiffness *Biomaterials* 273 120797.

31. Choi DH, Jeon B, Lim MH, Lee DH, Ye S-K, Jeong S-Y, Kim S. 2021 3D cell culture using a clinostat reproduces microgravity-induced skin changes. NPJ Microgravity 7 20.
32. Wrzesinski K, Frandsen HS, Calitz C, Gouws C, Korzeniowska B, Fey SJ. 2021 Clinostat 3D cell culture: protocols for the preparation and functional analysis of highly reproducible, large, uniform spheroids and organoids *Next Generation Culture Platforms for Reliable In Vitro Models: Methods and Protocols* (Springer) pp 17–62.
33. Navran S. The application of low shear modeled microgravity to 3-D cell biology and tissue engineering. Biotechnol Annu Rev. 2008;14:275–96.
34. Nguyen HD, Lin C-C. Viscoelastic stiffening of gelatin hydrogels for dynamic culture of pancreatic cancer spheroids. Acta Biomater. 2024;177:203–15.
35. Zhang J, Wehrle E, Adamek P, Paul GR, Qin X-H, Rubert M, Müller. R 2020 Optimization of mechanical stiffness and cell density of 3D bioprinted cell-laden scaffolds improves extracellular matrix mineralization and cellular organization for bone tissue engineering. Acta Biomater 114 307–22.
36. Martinez EM, Yoshida MC, Candelario TLT, Hughes-Fulford M. Spaceflight and simulated microgravity cause a significant reduction of key gene expression in early T-cell activation. Am J Physiology-Regulatory Integr Comp Physiol. 2015;308:R480–8.
37. Luo H, Wang C, Feng M, Zhao Y. Microgravity inhibits resting T cell immunity in an exposure time-dependent manner. Int J Med Sci. 2013;11:87.
38. Walther I, Pippia P, Meloni MA, Turrini F, Mannu F, Cogoli. A 1998 Simulated microgravity inhibits the genetic expression of interleukin-2 and its receptor in mitogen-activated T lymphocytes. FEBS Lett 436 115–8.
39. Ryu D, Kim D, Shim Y, Jin G, Mun S, Kim J, Yoon H-S, Cho SK, Kim H, Choi J-S, Yoo HJ, Bang S, Yang S-G. Cellular changes in an in vitro neural circuit system under simulated microgravity. Acta Biomater. 2025;204:446–56.
40. Morabito C, Lanuti P, Caprara GA, Marchisio M, Bizzarri M, Guarnieri S, Mariggiò. M A 2019 Physiological responses of jurkat lymphocytes to simulated microgravity conditions. Int J Mol Sci 20 1892.
41. Minopoli A, Evangelista D, Marras M, Perini G, Palmieri V, De Spirito M, Papi. M 2025 Viscoelastic interpretation of AFM nanoindentation for predicting nanoscale stiffness in soft biomaterials. Polym Test 153 109026.
42. Galluzzi M, Biswas CS, Wu Y, Wang Q, Du B, Stadler FJ. Space-resolved quantitative mechanical measurements of soft and supersoft materials by atomic force microscopy. NPG Asia Mater. 2016;8:e327–327.
43. Garcia R. Nanomechanical mapping of soft materials with the atomic force microscope: methods, theory and applications. Chem Soc Rev. 2020;49:5850–84.
44. Kontomaris SV, Malamou A, Stylianou A. 2024 Accurate Modelling of AFM Force-Indentation Curves with Blunted Indenters at Small Indentation Depths *Micromachines (Basel)*. 15.

45. Kontomaris SV, Malamou A, Stylianou A. 2022 The Hertzian theory in AFM nanoindentation experiments regarding biological samples: Overcoming limitations in data processing *Micron* 155 103228.
46. Kakarla AB, Kong I, Nukala SG, Kong. W 2022 Mechanical Behaviour Evaluation of Porous Scaffold for Tissue-Engineering Applications Using Finite Element Analysis. J Compos Sci 6 46.
47. Nguyen VB, Wang CX, Thomas CR, Zhang Z. Mechanical properties of single alginate microspheres determined by microcompression and finite element modelling. Chem Eng Sci. 2009;64:821–9.
48. Cai S, Hu Y, Zhao X, Suo. Z 2010 Poroelasticity of a covalently crosslinked alginate hydrogel under compression. J Appl Phys 108 113514.
49. Drury JL, Dennis RG, Mooney DJ. tensile Prop alginate hydrogels Biomaterials. 2004;25:3187–99.
50. Brat DJ, Bellail AC, Van Meir EG. The role of interleukin-8 and its receptors in gliomagenesis and tumoral angiogenesis. Neuro Oncol. 2005;7:122–33.
51. Wang J, Wang C, Sun Z, Zhang A, Niu Z, Zhang K, Wang S, Zhang C, Shi X, Yu D, Hou S, Lin. N 2025 CXCL8-dependent recruitment of neutrophils by the tumor microenvironment drives poor prognosis in glioblastoma patients. BMC Cancer 26 149.
52. Johnson DE, O'Keefe RA, Grandis JR. 2018 Targeting the IL-6/JAK/STAT3 signalling axis in cancer. Nat Rev Clin Oncol 15 234–48.
53. Young JS, Cho NW, Lucas C-HG, Najem H, Mirchia K, Chen WC, Tamaki C, Congivaram H, Seo K, Zakimi N, Daggubati V, Casey-Clyde T, Nguyen MP, Chen Z, Phillips JJ, Ozawa T, Aghi MK, Taylor JW, DeRisi JL, Bhaduri A, Berger MS, Heimberger AB, Butowski NA, Spitzer MH, Raleigh DR. 2026 IL6 Supports Development of an Immunosuppressive Microenvironment and Resistance to Therapy in Glioblastoma. Cancer Res 86 3570–87.
54. Lamano JB, Lamano JB, Li YD, DiDomenico JD, Choy W, Veliceasa D, Oyon DE, Fakurnejad S, Ampie L, Kesavabhotla K, Kaur R, Kaur G, Biyashev D, Unruh DJ, Horbinski CM, James CD. Parsa A T and Bloch O 2019 Glioblastoma-Derived IL6 Induces Immunosuppressive Peripheral Myeloid Cell PD-L1 and Promotes Tumor Growth. Clin Cancer Res 25 3643–57.
55. Carlini V, Noonan DM, Abdalalem E, Goletti D, Sansone C, Calabrone L, Albini. A 2023 The multifaceted nature of IL-10: regulation, role in immunological homeostasis and its relevance to cancer, COVID-19 and post-COVID conditions. Front Immunol 14.
56. Taga K, Tosato G. IL-10 inhibits human T cell proliferation and IL-2 production. J Immunol. 1992;148:1143–8.
57. D'Andrea A, Aste-Amezaga M, Valiante NM, Ma X, Kubin M, Trinchieri G. 1993 Interleukin 10 (IL-10) inhibits human lymphocyte interferon gamma-production by suppressing natural killer cell stimulatory factor/IL-12 synthesis in accessory cells. *J. Exp. Med.* 178 1041–8.

Figures

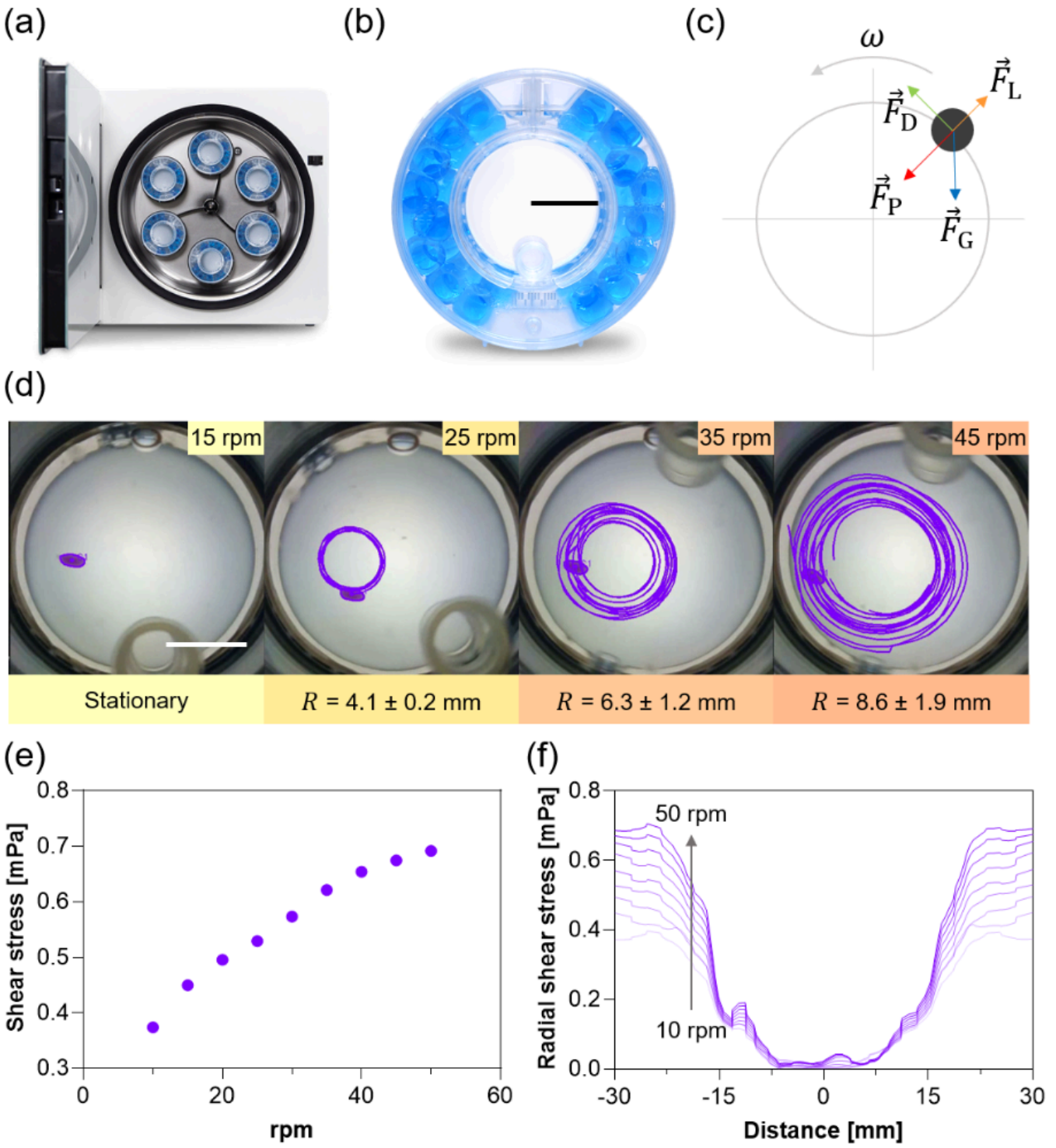


Figure 1

Hydrodynamic characterization of droplet motion under clinorotation. (a) Photograph of the ClinoStar clinostat bioreactor containing the rotating culture chambers. (b) Representative ClinoStar culture chamber used for clinostat culture of the bioprinted droplets. Scale bar: 30 mm. (c) Schematic representation of droplet motion during clinorotation. Vectors qualitatively represent the main force components governing droplet motion: gravity/buoyancy force , centripetal force associated with pressure gradient , drag force , and lift associated with velocity gradient . (d) SAM3-derived

trajectories of representative droplets at 15, 25, 35, and 45 rpm. Scale bar: 20 mm. (e) CFD-derived peripheral chamber-frame shear-stress intensity as a function of rotational speed. (f) CFD-derived radial distribution of chamber-frame shear-stress intensity at increasing rotational speeds.

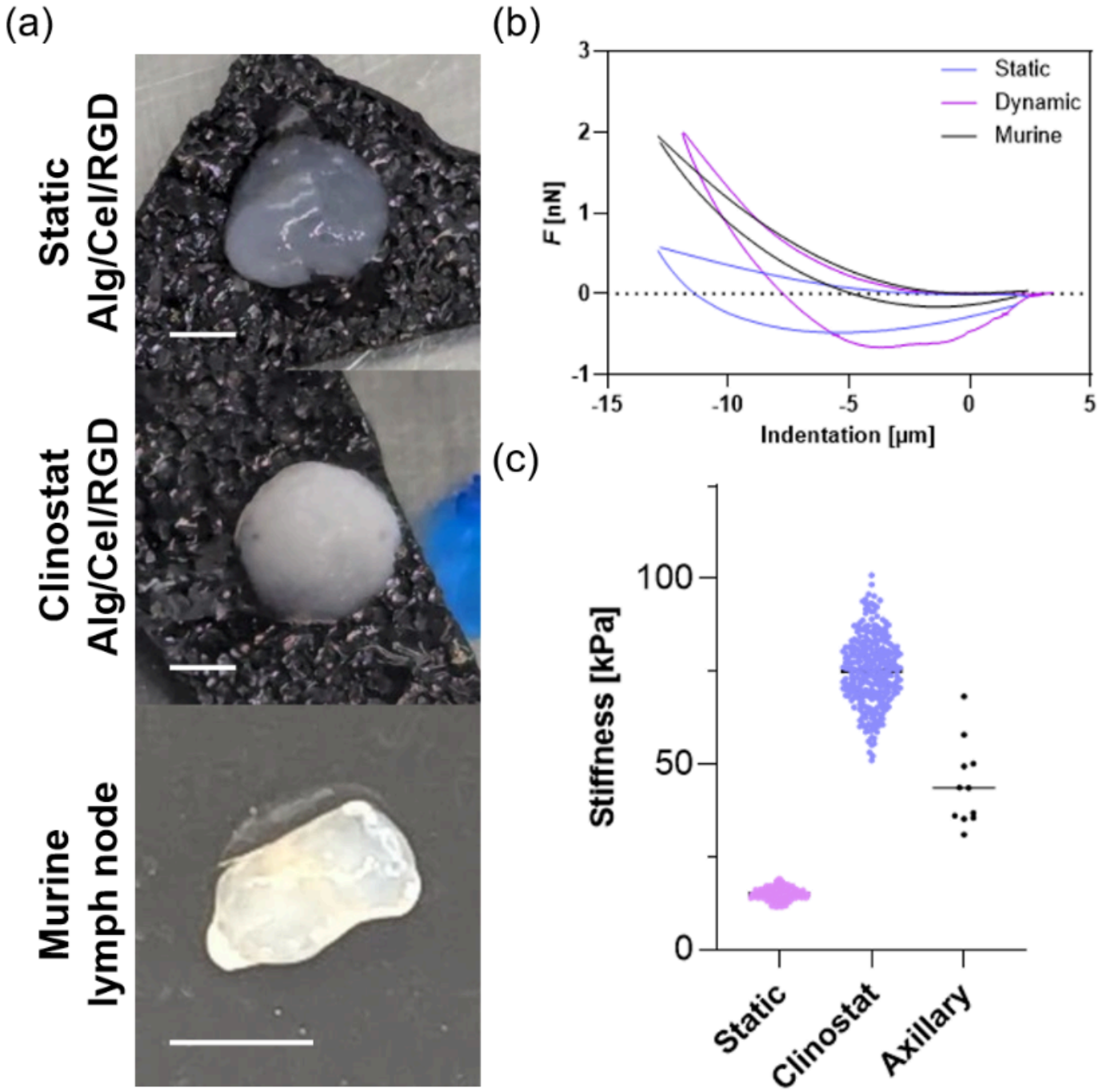


Figure 2

Local mechanical characterization of clinostat-conditioned Alg/Cel/RGD droplets and native murine axillary lymph nodes. (a) Representative photographs of 3D-bioprinted Alg/Cel/RGD droplets after 10

days of culture under static or clinostat conditions, together with representative murine axillary lymph node samples used as native tissue references. Scale bars: 2 mm. (b) Representative AFM force-indentation curves showing the higher local resistance to deformation of clinostat-cultured Alg/Cel/RGD droplets compared with static controls. (c) Apparent Young's modulus measured by AFM nanoindentation in static and clinostat-cultured Alg/Cel/RGD droplets and in native murine axillary lymph nodes.

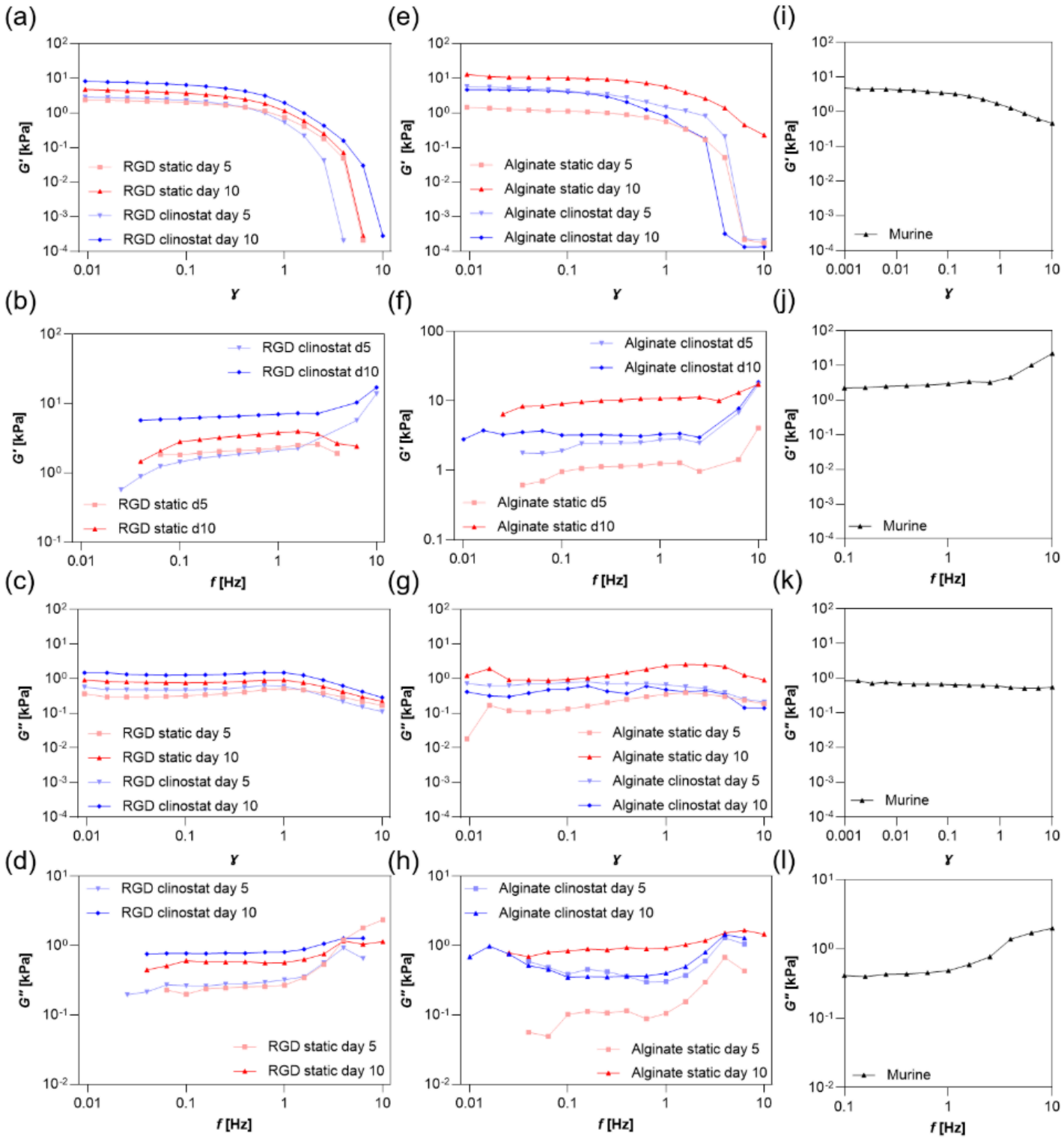


Figure 3

Bulk rheological characterization of (a-d) Alg/Cel/RGD and (e-h) alginate hydrogels cultured under static or clinostat conditions for 5 and 10 days, and of (i-l) native murine axillary lymph nodes. Oscillatory amplitude sweeps show the storage modulus (a,e,i) and loss modulus (c,g,k) as a function of strain amplitude, while oscillatory frequency sweeps show (b,f,j) and (d,h,l) as a function of frequency.

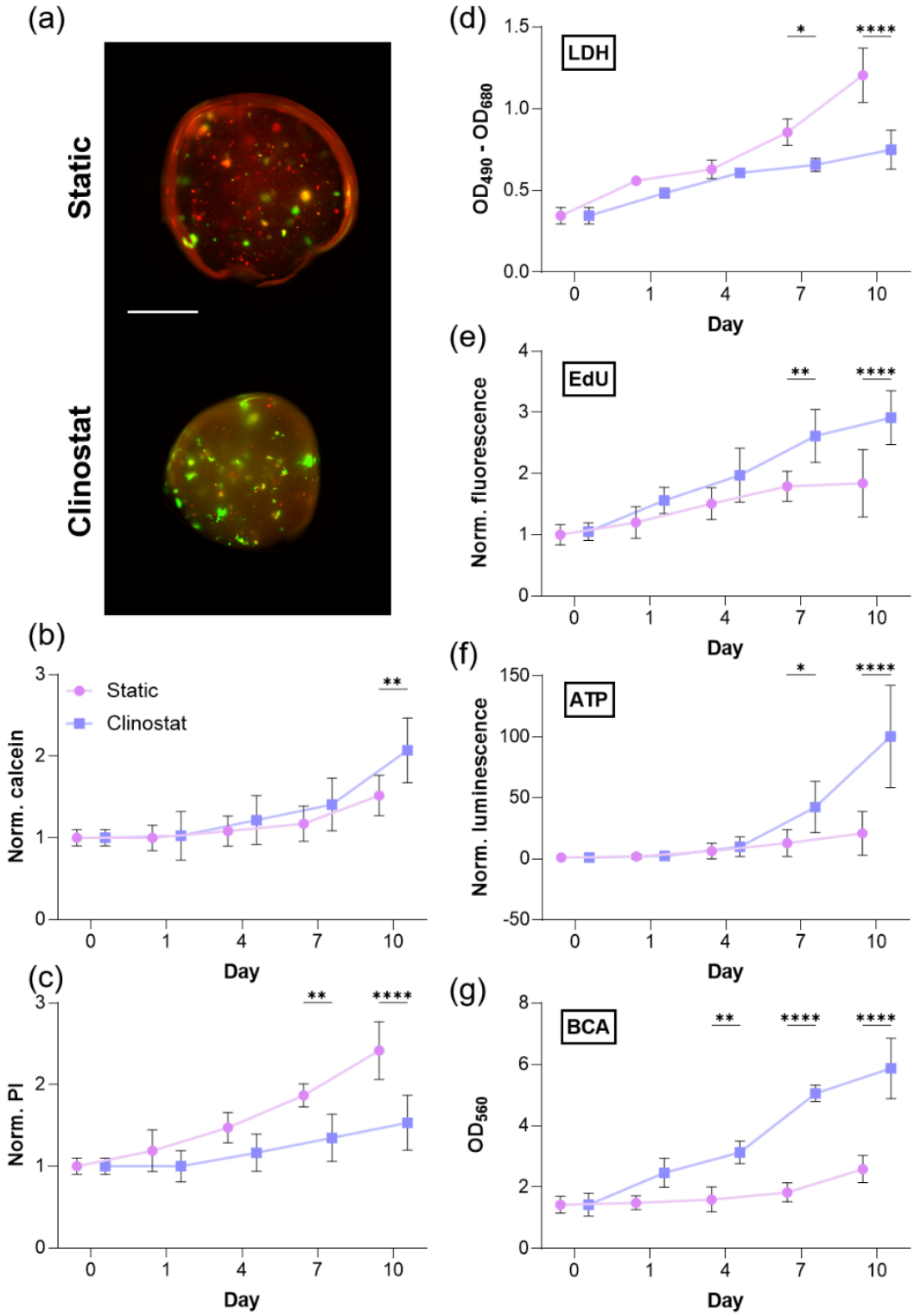


Figure 4

Clinostat culture supports Jurkat cell viability and metabolic activity within 3D-bioprinted droplets. (a) Representative Live/Dead fluorescence images of Jurkat-laden Alg/Cel/RGDdroplets cultured under static or clinostat conditions. Live cells are stained with calcein-AM (green), whereas dead or membrane-compromised cells are stained with PI (red). Scale bars: 2.5 mm. Evaluation of (b) calcein and (c) PI fluorescence intensity normalized to day 0. (d) LDH release, (e) EdU fluorescence intensity, (f) intracellular ATP level, and (g) total protein content (BCA assay). Normalized data are relative to day 0. Data are shown as mean values ± SD of n = 3 independent samples. All measurements were performed at days 0, 1, 4, 7 and 10. Symbols belonging to different conditions are slightly offset along the horizontal time axis for clarity, in order to avoid overlap of error bars. The legend shown in panel (b) applies to all panels.

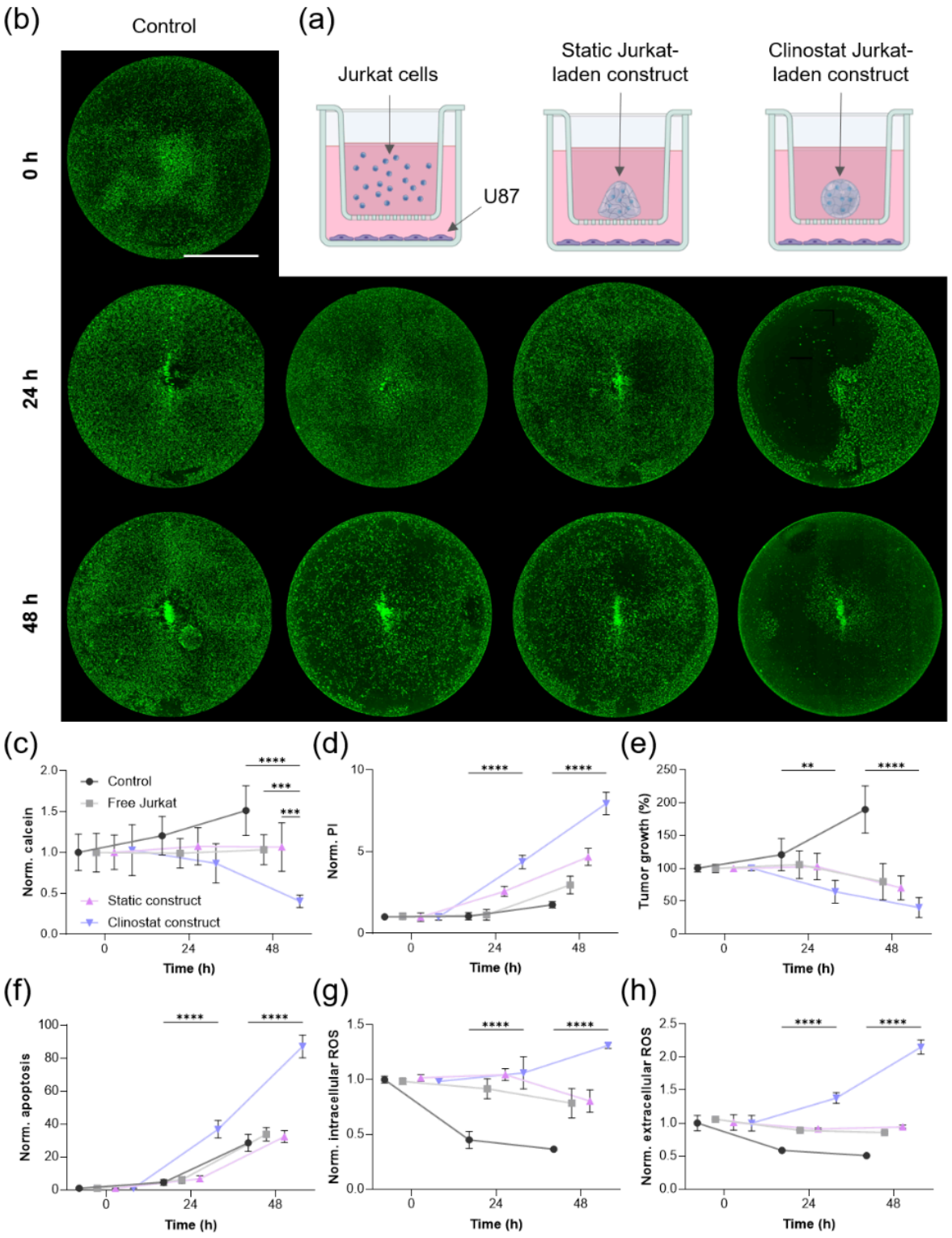


Figure 5

Jurkat-laden droplets previously cultured under clinorotation are associated with reduced U87 viability and increased apoptosis- and oxidative stress-associated signals in a transwell co-culture model. (a,b) Representative calcein fluorescence images of U87 glioblastoma cells during 48 hours of co-culture with Jurkat cells delivered in different formats as schematically shown in panel (a): Free Jurkat cells, static Jurkat-laden droplets, or clinostat-expanded Jurkat-laden droplets were transferred in the upper chamber

after 10 days of culture, while U87 cells were seeded in the lower chamber at a cell density of 5×10^4 cells per well. The 8 µm porous membrane allowed soluble-factor exchange and potential Jurkat migration toward the U87 monolayer. Scale bar: 5 mm. Integrated (c) calcein and (d) PI fluorescence intensity normalized to day 0. (e) U87 glioblastoma growth expressed as percentage of surface area occupied by calcein-positive U87 cells and normalized to the corresponding day 0 area. Data are presented as mean value ± SD of three independent experiments. (f) Quantification of apoptosis-associated fluorescence signal during 48 hours of co-culture. (g) Intracellular ROS levels in U87 cells measured using the CellROX assay. (h) Extracellular ROS levels measured in culture supernatants during the Jurkat/U87 interaction assay. Data are presented as mean ± SD of *n* = 3 independent experiments. All measurements were performed at 0, 24 and 48 hours. Symbols belonging to different conditions are slightly offset along the horizontal time axis for clarity, in order to avoid overlap of error bars. The legend shown in panel (c) applies to all panels.

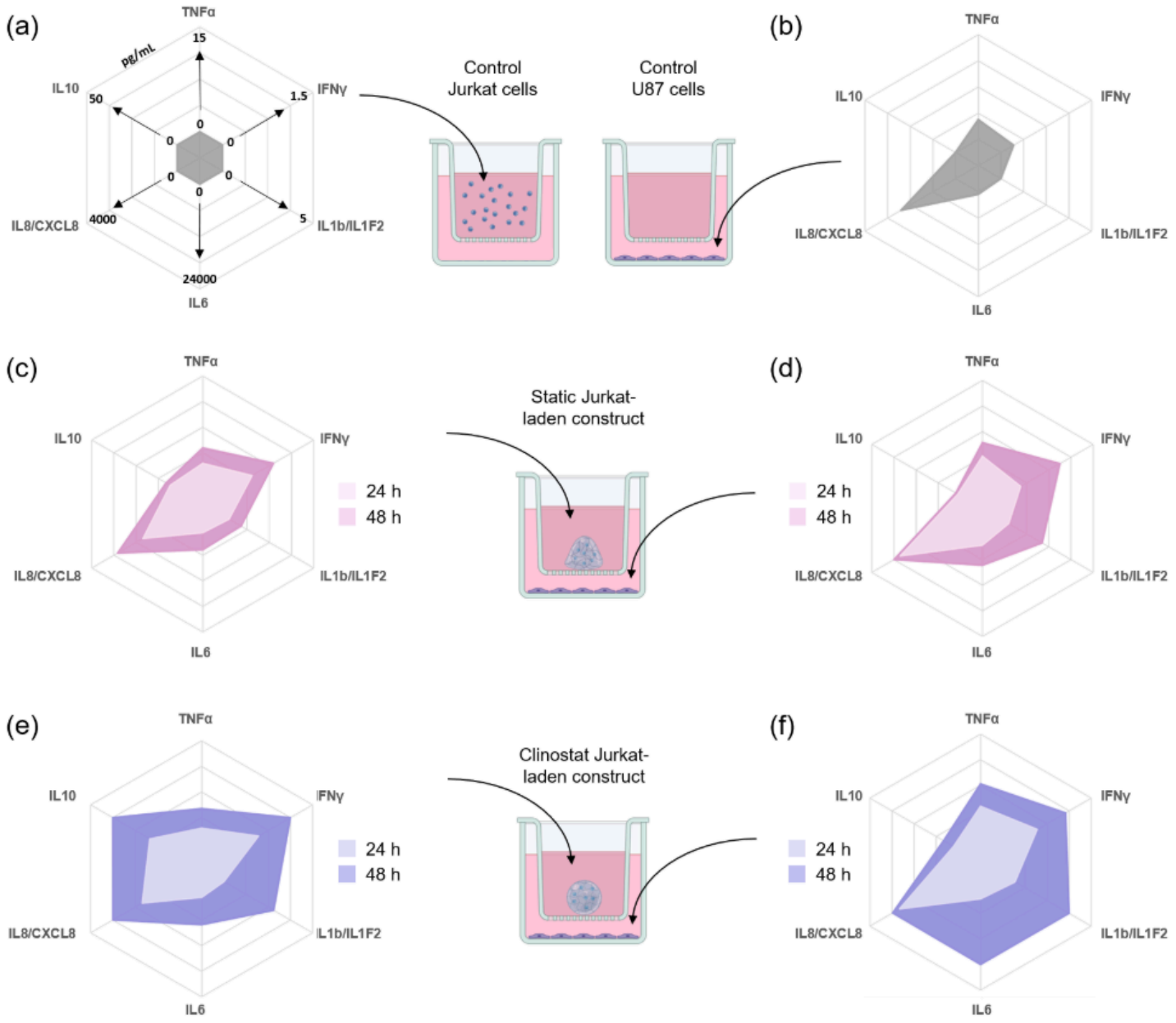


Figure 6

Multiplex cytokine profiling during the Jurkat/U87 interaction assay. Cytokine levels were measured over 48 hours using a Luminex bead-based multiplex immunoassay. Radar plots show the cytokine profiles of TNF-α, IFN-γ, IL-1β/IL1F2, IL-6, IL-8/CXCL8, and IL-10 in the different experimental conditions. Control profiles were obtained from (a) Jurkat and (b) U87 cells cultured without cross-contamination in the upper and lower transwell compartment, respectively. Cytokine levels were measured in supernatants collected from both (c,e) upper and (d,f) lower transwell compartment for static and clinostat droplets. Cytokine ranges are reported in panel (a). Data are reported as mean cytokine concentrations of $n = 3$ independent samples.